Originally published in Plasma Phys. Control. Fusion **62** 085015, © The Authors, 2020
Original Content from this work may be used under the terms of the Creative Commons Attribution 4.0 licence. Any further distribution of this work must maintain attribution to the author(s) and the title of the work, journal citation and DOI.
doi:10.1088/1361-6587/ab9a62

Collisional effects on the electrostatic shock dynamics in thin-foil targets driven by an ultraintense short pulse laser

A Sundström[1], L Gremillet[2,3], E Siminos[4] and I Pusztai[1]

[1] Department of Physics, Chalmers University of Technology, SE-412 96 Göteborg, Sweden
[2] CEA, DAM, DIF, F-91297 Arpajon, France
[3] Université Paris-Saclay, CEA, LMCE, F-91680 Bruyères-le-Châtel, France
[4] Department of Physics, Gothenburg University, SE-412 96 Göteborg, Sweden

E-mail: andsunds@chalmers.se

Abstract. We numerically investigate the impact of Coulomb collisions on the ion dynamics in high-Z, solid density caesium hydride and copper targets, irradiated by high-intensity ($I \approx 2{-}5 \times 10^{20}\,\mathrm{Wcm^{-2}}$), ultrashort ($\sim$10 fs), circularly polarized laser pulses, using particle-in-cell simulations. Collisions significantly enhance electron heating, thereby strongly increasing the speed of a shock wave launched in the laser-plasma interaction. In the caesium hydride target, collisions between the two ion species heat the protons to $\sim$100$-$1000 eV temperatures. However, in contrast to previous work (A.E. Turrell *et al.*, 2015 *Nat. Commun.* **6** 8905), this process happens in the upstream only, due to nearly total proton reflection. This difference is ascribed to distinct models used to treat collisions in dense/cold plasmas. In the case of a copper target, ion reflection can start as a self-amplifying process, bootstrapping itself. Afterwards, collisions between the reflected and upstream ions heat these two populations significantly. When increasing the pulse duration to 60 fs, the shock front more clearly decouples from the laser piston, and so can be studied without direct interference from the laser. The shock wave formed at early times exhibits properties typical of both hydrodynamic and electrostatic shocks, including ion reflection. At late times, the shock is seen to evolve into a hydrodynamic blast wave.

arXiv:2002.10935v3 [physics.plasm-ph] 30 Jul 2020

1. Introduction

The use of lasers to accelerate ions is a field of intense research [1], with many demonstrated or envisioned applications, such as imaging of electromagnetic fields in plasmas [2, 3], creation of warm dense matter [4–6], production of intense neutron sources [7], material testing [8, 9], laboratory astrophysics [10], and ion-beam therapy [11, 12]. Among the few laser-based ion acceleration mechanisms considered so far, including the extensively studied, and particularly robust, target normal sheath acceleration (TNSA), collisionless shock acceleration (CSA) is of particular interest due to its potential to produce a relatively narrowly peaked ion energy spectrum [13–18]. Collisionless shocks also play a role in particle energization in astrophysical plasmas [19, 20].

As the shock front passes by, the plasma is rapidly compressed and directional kinetic energy is converted into thermal energy. This can take place either through collisional processes, such as in hydrodynamic shocks – relevant in, e.g., inertial fusion plasmas [21, 22] and relativistic laser-plasma experiments [23] – or collisionless mechanisms, involving longitudinal electrostatic fields generated by space charge effects from shock compression [14]. Collisionless shocks can also hinge upon self-generated magnetic fields, such as those resulting from the Weibel instability [24, 25], yet such shocks, of turbulent character, develop at Mach numbers much larger than those of the laminar electrostatic shocks that we shall address here [26]. In relativistic laser-plasma interactions, electrostatic shocks can arise either from the forward push exerted by the laser's ponderomotive force (or "laser piston") [14] in the radiation pressure acceleration (RPA) regime, or from electron pressure gradients in nonuniform plasmas [17]. While "collisionless shocks", as the name suggests, are sustained through collective collisionless plasma processes, Coulomb collisions may play a role in their dynamics. Indeed, a finite collisionality, while affecting the shock, does not necessarily disrupt it [27].

Although the effect of collisions is often deemed negligible in high-intensity laser-plasma interactions, due to the high particle energies at play, it can become important when using solid or near-solid density targets, especially if they contain elements of high atomic numbers. In this paper, we consider two scenarios where collisions play an important role: one has basic science interest while the other is relevant for high energy density applications. We also present cases with parameters in between, to clarify how changes in laser and target parameters affect the ion dynamics, and in particular the properties of the resulting electrostatic shocks. In all cases, we will consider a circularly polarized femtosecond ($10-60\,\mathrm{fs}$) laser pulse.

The first case we consider is motivated by the work by Turrell, Sherlock & Rose [28] (hereafter referred to as TSR), where it was reported that inter-species collisions in a caesium hydride (CsH) target induce ultrafast collisional ion heating, and essentially affect the shock dynamics. We find significantly different results compared to what is reported by TSR, even though we study essentially the same physical setup. Importantly, we do not observe the occurrence of ultrafast proton heating downstream of the shock, as most of the protons are reflected, and as such, there is no appreciable inter-species friction in the downstream. As we will discuss, this discrepancy is likely due to a different behaviour, at the high densities considered, of the different collision algorithms employed by TSR and us.

The other case we address was first considered in a recent study of ours [29] investigating ionization and collisional electron heating effects in solid copper targets, relevant for warm-dense-matter generation. Here, we focus on the ion dynamics and examine the impact on the generated shock of the increased electron density in copper compared to CsH. We also assess the sensitivity of the ion dynamics to the laser parameters and target thickness.

When using circular laser polarization, collisions dominate the electron heating, which, in turn, results in the formation of a stronger electrostatic shock compared to

a purely collisionless simulation. In the scenarios with copper, the evolution of the shock is studied, from a hybrid hydrodynamical–electrostatic shock, through a gradual dissipation of its energy, to the transition to a hydrodynamical blast wave. In particular, the onset of shock ion-reflection is found to be self-amplifying. Collisional friction between the upstream and reflected ions heats the upstream ion population, which enhances the fraction of reflected ions.

2. Simulation study

In this paper, we investigate two different target materials, caesium hydride (CsH) and pure copper (Cu), both at their respective solid densities. We perform one-dimensional (1D) particle-in-cell (PIC) simulations with the Smilei PIC code [30] (version `4.1`), which has a collision module that has been benchmarked [31] in the high-density/low-temperature regimes relevant for this paper. In all cases, we use a circularly polarized (CP), $\lambda = 800\,\mathrm{nm}$ wavelength laser with a Gaussian temporal profile. The simulation box consists of 51200 cells over a length of $20\,\mu\mathrm{m}$ (resolution $\Delta x = 0.39\,\mathrm{nm}$), and a 4^{th} order interpolation shape function is employed. The use of a high-order shape function ensures good energy conservation despite the Debye length in our collisionless simulation being somewhat lower than the mesh size. The electrons are initialized at a temperature of $T_{\mathrm{e},0} = 1{-}10\,\mathrm{eV}$ and the ions at a temperature of $0.1{-}1.0\,\mathrm{eV}$.

Both target materials contain a highly charged, Z^*, ion species, such that the effect of collisions is significant. This high collisionality turns out to be of crucial importance for the electron heating. Since CP is used, the target electrons are energized through inverse Bremsstrahlung rather than from the strongly inhibited $j{\times}B$ [32] or vacuum heating [33,34] mechanisms. In our recent work [29], we showed that collisional electron heating produces well-thermalized electron populations with temperatures in the $\sim 1{-}10\,\mathrm{keV}$-range.

The use of the CsH target was inspired by the work by TSR [28]. As a target material, CsH could be of interest for laser acceleration of protons since it contains hydrogen volumetrically, like a plastic target. An advantage of this material over plastic, though, is the much higher ionization degree (Z^*) that can be reached, hence enhancing collisional effects. Although practically challenging, due to the high chemical reactivity of CsH and difficulties in the target fabrication, it would, in principle, be possible to use this material in an experiment.

The CsH target is composed of an equal number mixture of protons and caesium ions. The charge state of the Cs ions is set to a fixed value of $Z^* = 27$, corresponding to full ionization of the three outermost shells. The resulting quasi-neutral electron density is $n_{\mathrm{e},0} = 250\,n_{\mathrm{c}}$, where $n_{\mathrm{c}} = \epsilon_0 m_{\mathrm{e}}\omega^2/e^2 \approx 1.7 \times 10^{21}\,\mathrm{cm}^{-3}$ is the critical density (ϵ_0 is the vacuum permittivity, m_{e} is the electron mass, ω is the laser frequency and e is the elementary charge), corresponding to a collisionless skin depth of $l_{\mathrm{s}} = 8.0\,\mathrm{nm}$ which is well resolved. The target thickness is 300 nm, as in the simulations of TSR.

Copper, on the other hand, lacks the embedded protons but is, from a practical

standpoint, much more readily available as a target material. Copper is also relatively highly charged, and hence presents a collisionality comparable to CsH. The lack of embedded protons‡ makes copper less suitable for volumetric proton acceleration, but its high collisionality could be beneficial for other applications, such as warm-dense-matter generation [29]. In the simulations, the copper ions are initialized with three fully ionized atomic shells ($Z^* = 27$), and at solid density (corresponding to $n_{\mathrm{e},0} = 1307\, n_{\mathrm{c}}$ and $l_{\mathrm{s}} = 3.5\,\mathrm{nm}$). This choice is informed by simulation results for a copper target including field and collisional ionization processes, analyzed in Ref. [29], showing that the average Z^* rapidly reaches this value, then it stagnates, due to a significant jump in ionization energy beyond the three atomic shells. We found that retaining the ionization dynamics has no significant impact on the ion dynamics.

With the copper targets, two different target thicknesses and two different laser parameters were considered. The thinner target is 300 nm thick, as in the CsH simulations, which has the advantage of quicker heating and homogenization compared to a thicker target. The thicker (2.5 µm) target, on the other hand, can be more suitable for warm-dense-matter applications: A high energy density will be maintained over a longer time since hydrodynamic expansion takes longer to reach the interior of a thicker target. We note that at the high densities and ionization degrees considered here, the useful lifetime of the target can also be affected by radiative losses, dominantly through Bremsstrahlung at the temperatures of interest. We find, however, that for our parameters, the radiative cooling time is typically of several picoseconds, so that Bremsstrahlung losses should not greatly impact the plasma dynamics during the integration time ($\leq$1 ps) of our simulations. For the same reason, internal radiative energy transport was also not modelled in the simulation.

We considered two different sets of laser parameters: an amplitude of $a_0 = 15$ ($I \approx 5 \times 10^{20}\,\mathrm{Wcm^{-2}}$) and full-width-at-half-maximum (FWHM) duration of 10 fs, as well as $a_0 = 10$ ($I \approx 2 \times 10^{20}\,\mathrm{Wcm^{-2}}$) and a FWHM duration of 60 fs. The former is used with both the CsH and Cu thin targets, and the latter is used for both the thin and thick Cu targets. The use of thicker targets goes along with increased integration times, allowing a larger number of fast particles to reach the domain boundaries. To keep them inside the domain, the thicker target is initialized with its front at $x = 7.5\,\mu\mathrm{m}$ compared to the other targets located at 1 µm.

For an accurate modelling of Coulomb collisions, employing the relativistic PIC algorithm of [31] (to be further discussed in Sec. 3.2), a relatively high number of particles per cell is needed. In the thinner target, 500 macro-particles per species per cell was used, while in the thicker target, the particle number was reduced somewhat to 400 macro-particles per species per cell. Resolution tests, with halved particle number or halved spatial resolution (with same total number of particles), for the Cu thin target simulation show that the simulations are numerically converged.

‡ The copper is also modelled without any proton contamination layer on the surfaces. While such a contamination layer would affect the TNSA process, and somewhat the laser absorption, it is not expected to have a significant impact on the shock dynamics, that is the focus of this paper.

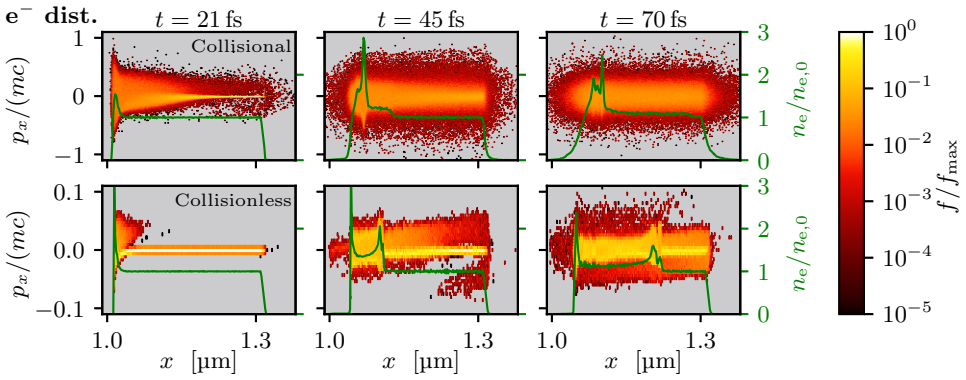


Figure 1. Electron distributions at (left) and after the laser peak intensity (middle and right), with (top) and without (bottom) collisions, using CP. Green curve: electron density. Please note the different momentum scales for the collisional and collisionless simulations.

3. Ion dynamics in the CsH target

Motivated by the previous work by TSR, we performed a similar set of simulations in CsH. However, despite virtually identical setups, our results differ significantly from the ones by TSR.

3.1. Comparison of collisional and collisionless results

The primary effect of the strong target collisionality is to significantly enhance electron heating through inverse Bremsstrahlung [29]. As an illustration of the collisional electron heating, Fig. 1 shows the electron phase space of the collisional (top row) and collisionless (bottom row) CsH simulations at three successive times: during peak laser intensity at $t = 21\,\mathrm{fs}$, right after the laser pulse has ended at $t = 45\,\mathrm{fs}$, and even later at $t = 70\,\mathrm{fs}$. In figures hereafter, the phase space distribution functions f are normalized to the maximum value of each respective *initial* Maxwellian distribution, $f_{\max}$.

The electrons in the target front layer are energized in the transverse (y-z) plane by the laser electric field. Then collisions scatter their momentum into the longitudinal direction, as seen through the large spread in p_x near the plasma front in the $t = 21\,\mathrm{fs}$ frame of the collisional distribution. Collisions then entail a fast thermalization of the electrons to a Maxwellian distribution, yielding a bulk temperature of $T_\mathrm{e} \approx 10\,\mathrm{keV}$ that corresponds to an ion-acoustic speed of $c_\mathrm{s} \approx (Z^*_\mathrm{Cs} T_\mathrm{e}/m_\mathrm{Cs})^{1/2} \approx 1.5 \times 10^{-3} c$, where c is the speed of light in vacuum.

The electron density is also indicated in Fig. 1 (green solid curve, right axis). Compared to the collisionless case, the collisional simulation shows smoother spatial structures likely due to a combination of higher temperature, collisional dissipation and dispersion of non-linear waves. The Debye length is $\lambda_\mathrm{D} \approx 1\,\mathrm{nm}$ and $\lambda_\mathrm{D} \approx 0.1\,\mathrm{nm}$ in the collisional and collisionless cases, respectively. The collisional electron density profile also shows signs of an electrostatic shock wave: a density jump moving away from the

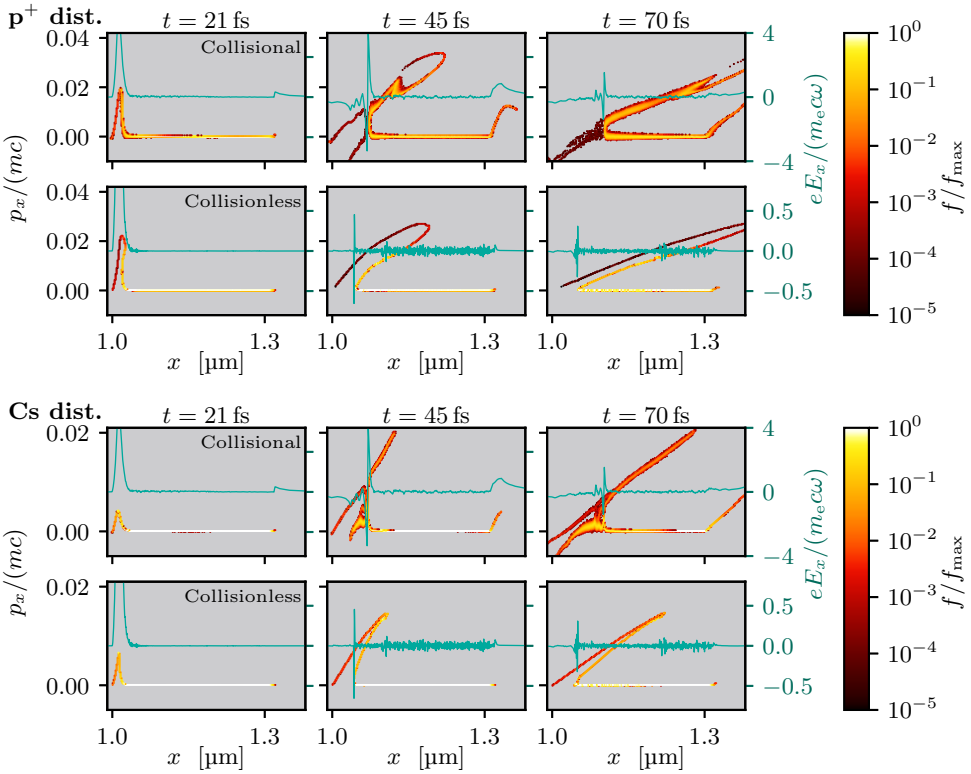


Figure 2. Proton (top frame) and caesium ion (bottom frame) distributions in the 300 nm CsH target at peak laser intensity ($t = 21$ fs) and after the pulse has passed ($t = 45$ fs and 70 fs), with (upper panels) and without (lower panels) collisions, using CP. The longitudinal electric field is also plotted (turquoise solid line, right axes). Note the different electric field scales between the collisional and collisionless panels.

target front is visible in the $t = 45$ fs and 70 fs panels. In the collisionless case, the density profile exhibits two peaks in both time frames. The rightmost density jump is due to the leading edge of the radiation-pressure-accelerated Cs ions (Fig. 2), while the leftmost density peak corresponds to an electrostatic shock, which, due to the low electron temperature, is too slow for its propagation to be noticeable over the displayed time and length scales.

In Fig. 2, the evolution of the ion distributions in the collisional and collisionless CsH targets are shown. The top frame shows the proton, the lower one the Cs ion phase spaces, with the upper (lower) rows in both frames corresponding to the collisional (collisionless) simulations, at times $t = 21$ fs, $t = 45$ fs and $t = 70$ fs. At $t = 21$ fs, the difference between the collisional and collisionless simulations is quite small; in both cases, the protons and Cs ions are pushed by the laser piston. However, due to the lower charge-to-mass ratio of the Cs ions compared to the protons, the Cs ions react more slowly to the radiation pressure (RP) induced electrostatic field (at $x \approx 1$ µm) than the protons, as seen by the almost four times higher velocity reached by the protons ($p_x/mc \approx 0.02$) at $t = 21$ fs. Owing to the short pulse duration (10 fs), the Cs ions do not have enough time to react to RP before the pulse ends.

Also shown in Fig. 2 is the longitudinal electric field, E_x (turquoise curve), normalized to $m_e c\omega/e \approx 4.013 \times 10^{12}\,\mathrm{V/m}$. The charge separation during the RPA phase creates a strong longitudinal electric field, visible as a positive spike in E_x close to $x = 1\,\mu\mathrm{m}$ in the $t = 21\,\mathrm{fs}$ panels. Note that the peaks of the RP field are cut off in the display. The collisionless RP field reaches a normalized amplitude of $eE_x/(m_e c\omega) = 8.6$, while the field in the collisional simulation reaches only 5.6. However, the RP field in the collisional simulation has a wider spatial extent. When the electric field is integrated, the potential drop across the RP field is $e\phi \approx 220\,\mathrm{keV}$ and $280\,\mathrm{keV}$ in the collisionless and collisional cases, respectively. Thus, collisions do not affect the RPA process significantly, as apparent from the comparison of the collisional and collisionless panels at $t = 21\,\mathrm{fs}$ in Fig. 2.

With collisions, the electrostatic structure caused by RPA transforms into an electrostatic shock, as evidenced by the single strong oscillation of E_x and modulations in the downstream ion distribution in the $t = 45\,\mathrm{fs}$ and $70\,\mathrm{fs}$ frames of Fig. 2. A close inspection of the collisionless simulation reveals the same behaviour (although barely visible in Fig. 2), indicating that an electrostatic shock has also formed there. However, due to the high electron temperature from collisional heating, the shock is much stronger and faster in the collisional case. In absolute units, the average shock velocity between $t = 45\,\mathrm{fs}$ and $70\,\mathrm{fs}$ was $v_{\mathrm{sh}}/c \approx 4.3 \times 10^{-3}$ and $v_{\mathrm{sh}}/c \approx 0.9 \times 10^{-3}$ in the collisional and collisionless simulations, respectively. Yet, the higher electron temperature in the collisional target ($T_e \approx 10\,\mathrm{keV}$ vs. $T_e \approx 0.2\,\mathrm{keV}$) leads to a lower Mach number ($\mathcal{M} \approx 2.9$ vs. $\mathcal{M} \approx 4$). The low shock speed in the collisionless simulation implies that the shock-reflected ions have a significantly lower energy compared to those originating from the initial burst of the RPA. In both the collisional and collisionless cases, given its limited energy reservoir provided by the ultrashort ($10\,\mathrm{fs}$) laser pulse, the shock wave steadily loses its energy, as seen by the declining field amplitude and the sloped reflected ion structure in the proton and Cs phase spaces (i.e. the shocks are losing speed).

Another consequence of the efficient inverse Bremsstrahlung electron heating is that the collisional simulation displays TNSA at the target rear boundary, whereas it is virtually nonexistent in the collisionless simulation, as evident at $t = 70\,\mathrm{fs}$ in Fig. 2. Due to the use of CP, the electrons are weakly energized in the collisionless case, hence quenching TNSA. In the collisional simulation, the TNSA protons attain energies slightly lower than the RPA protons at the final simulation time.

In the collisional case, we also see that the reflected and upstream proton and Cs ion populations are being significantly heated, in contrast to their collisionless counterparts. By fitting Maxwellians to the proton distribution in the range $x = 1.15{-}1.18\,\mu\mathrm{m}$ (close to, but still beyond direct influence from the shock front) at time $t = 70\,\mathrm{fs}$, the upstream proton population is found to have already been heated to $T_{\mathrm{p}}^{(\mathrm{u})} = 120\,\mathrm{eV}$, while the reflected protons are at a temperature of $T_{\mathrm{p}}^{(\mathrm{r})} = 750\,\mathrm{eV}$. We recall that the initial ion temperature was $0.1\,\mathrm{eV}$. Simulations in which various types of collisions (e.g., proton–Cs or ion–electron) have been selectively switched off (not shown here), reveal that the heating of the reflected ions proceeds from their friction with the background Cs ions,

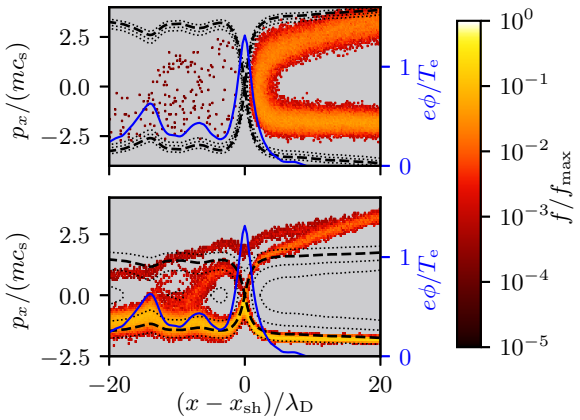


Figure 3. Proton (top panel) and Cs ion (bottom panel) distributions in the shock frame of reference at $t = 70\,\mathrm{fs}$, together with the shock electrostatic potential, $e\phi/T_\mathrm{e}$ (blue solid line, right axes), using $T_\mathrm{e} = 10\,\mathrm{keV}$. Also shown are contours of constant energy, $\mathcal{E} = mv^2/2 + eZ(\phi - \phi_\mathrm{max})$ (black, dashed or dotted lines). The black dashed line corresponds to $\mathcal{E} = 0$ at the potential peak, ϕ_max.

while the upstream ions are mainly collisionally heated by the fast electrons.

To get a more detailed picture of the vicinity of the electrostatic shock front, close-ups of the proton (top) and Cs (bottom) distributions, at $t = 70\,\mathrm{fs}$, are displayed in Fig. 3. The distributions have been shifted to the shock rest frame (at velocity $v_\mathrm{sh}/c \approx 3.1 \times 10^{-3}$), relative to the position of the potential maximum, x_sh; the velocities are normalized to the ion-acoustic sound speed, c_s. The electrostatic potential, $\phi(x) = -\int_{x_0}^{x} E_x(x')\,\mathrm{d}x'$, where x_0 is such that ϕ averages to zero in the range $8 \leq (x - x_\mathrm{sh})/\lambda_\mathrm{D} \leq 10$§, is also plotted (blue line), along with corresponding constant energy contours (black dashed or dotted lines). The black dashed line represents the constant energy contour which has zero (shock-frame) kinetic energy at the peak of ϕ. This line is an approximate boundary between the reflected and passing ions; in a steady state, this would be a separatrix. The top frame shows that almost all protons are located within the reflected region of phase space. Meanwhile, only around 5−10% of the Cs ions are reflected, and accordingly, the upstream Cs distribution mostly lies below the passing–reflected boundary. The difference in ion reflection between the two ion species is due to their different charge-to-mass ratios [35].

The electrostatic potential is seen to oscillate downstream of the shock (left side in Fig. 3), which creates regions of ion trapping. In a perfectly steady-state and collisionless electrostatic shock, these regions would be empty, as there would be no means for the ions to cross the separatrix. However, due to the slowly decreasing amplitude and speed

§ In an idealized electrostatic shock, $\phi \to 0$ as $x \to \infty$. However, in practice, the electrostatic potential presents spatial variation even well upstream of the shock front, from sources other than the shock, which motivates this averaging procedure. The choice of the x-range to average over is somewhat arbitrary, but it is chosen reasonably close to the shock front, while sufficiently outside the shock width.

of the shock, the trapping regions experience a steady influx of Cs ions. These adiabatic effects are likely more important here than collisional scattering [27]. While the Cs ions mainly enter the trapping regions from the leftmost potential hump in Fig. 3, almost no protons pass the shock front and hence only few protons ever enter the trapped region. The protons trapped in those regions are mostly remnants of the protons left behind the main RPA (seen to the left of the shock front in the $t = 45\,\mathrm{fs}$ frame of Fig. 2).

3.2. Ultrafast ion heating revisited

The theoretical study of TSR [28] predicts that an ultrafast collisional ion heating may take place in plasmas composed of light and heavy ion species. This result is born out by 1D collisional PIC simulations performed with the EPOCH [36] code, considering a CsH target almost identical to that in the current paper. The authors ascribe the observed ultrafast heating to collisional friction between the protons and Cs ions as they experience a differential acceleration in the electrostatic field of the shock.

The CsH setup presented in this paper is almost identical to that of TSR – apart from a mere 1% difference in the electron density, the laser polarization and the increased resolution in our case. We have also run a Smilei simulation with exactly the same physical parameters (including linear polarization and numerical resolution) as TSR. As regards the ion dynamics, this simulation yields results virtually identical to the CsH simulation presented in Fig 2 (therefore, they are not presented here separately). However, none of our simulations reproduce the main findings of TSR, namely, the collisional downstream proton heating ascribed to inter-species ion friction and the absence of ion reflection. By contrast, our simulations indicate that the collisional interaction between the ion species does not inhibit the proton reflection; in fact, as shown in e.g. Fig. 3, nearly all protons are reflected, and these are subsequently heated through collisional friction through the ambient (upstream) Cs ions. The proton heating is strongest in the *reflected* ion population.

The PIC results of TSR are interpreted by a two-fluid model retaining the momentum and energy moments of the Fokker-Planck equation, assuming Maxwellian distributions. It provides steady-state expressions for the longitudinal derivatives of the temperatures and velocities of the two fluid species, which are then integrated over the spatial width of the shock front. The energy input to the system comes from an electric field term representing the electrostatic shock field. Importantly, the possibility of ion reflection is ruled out by construction: protons are forced to pass through the barrier and gain all the available potential energy, which is consistent with their simulation results, but not with ours. In the collisionless case the protons should clearly be reflected due to their higher charge to mass ratio than that of Cs. The only way to avoid proton reflection is if a very strong friction between the two species pulls the ions across the potential barrier. This, however, requires a much stronger collisional coupling than what we observe.

Thus, we believe that the difference between TSR's results and ours is (at least

partly‖) a consequence of the different collision algorithms used. The version of the Epoch [36] code used by TSR was equipped with a collision module based on the algorithm proposed by Sentoku & Kemp [37] (SK), while Smilei employs the scheme developed by Pérez et al. [31] (NYP), which generalizes the Nanbu & Yonemura scheme [38,39] to the relativistic regime. Both collision models are designed to reproduce the Fokker–Planck limit, where small-angle collision events dominate, which is relevant for high-temperature and/or low-density plasmas. However, at the high plasma densities considered here, which are susceptible to quantum degeneracy and coupled plasma effects, corrections must be made to avoid unphysically high collision frequencies¶. This is also a major point where the SK and NYP algorithms differ.

In the high-density/low-temperature regime, the SK model forces the effective temperature of the interacting species to stay above the Fermi temperature, in order to emulate the Fermi-degenerate regime. This leads to the maximum collision frequency $\hat{\nu}^{(\mathrm{SK})}_{\alpha\beta} = m_\mathrm{e} Z^*_\beta e^4 \log\Lambda/(12\pi^3\epsilon_0^2\hbar^3)$ between two particles of species α and β [37, eq. (10)]. By contrast, drawing from the prescription of Ref. [41] for coupled plasmas, the NYP model applies a lower bound on the collisional mean free path, which can never get smaller than the mean inter-particle distance $r_\beta \sim (4\pi n_\beta/3)^{-1/3}$. This yields the saturated collision frequency $\hat{\nu}^{(\mathrm{NYP})}_{\alpha\beta} = (4\pi n_\beta/3)^{1/3}(T_\alpha/2m_\alpha)^{1/2}$ [31, sec. I-C].

At the considered ion density ($n_\mathrm{Cs} = 1.5\times10^{28}\,\mathrm{m}^{-3}$) and a representative ion temperature of $T_\mathrm{i} = 100\,\mathrm{eV}$, we find $\nu^{(\mathrm{Spitzer})}_{\mathrm{p\,Cs}} \approx 1.5\times10^{15}\,\mathrm{s}^{-1}$, and $\lambda_{\mathrm{p\,Cs}} \approx 0.06\,\mathrm{nm}$ that is significantly smaller than the inter-atomic distance $\sim$0.2 nm. Thus the dense-plasma limit of NYP should hold under such conditions but not the degenerate SK limit. One thus obtains that $\nu^{(\mathrm{SK})}_{\mathrm{p\,Cs}} = \nu^{(\mathrm{Spitzer})}_{\mathrm{p\,Cs}} \approx 1.5\times10^{15}\,\mathrm{s}^{-1}$ is more than 5 times larger than the dense-plasma value $\nu^{(\mathrm{NYP})}_{\mathrm{p\,Cs}} \approx 2.7\times10^{14}\,\mathrm{s}^{-1}$. This discrepancy is only strengthened when considering Cs–Cs collisions. Again at $n_\mathrm{Cs} = 1.5\times10^{28}\,\mathrm{m}^{-3}$ and $T_\mathrm{i} = 100\,\mathrm{eV}$, one finds $\nu^{(\mathrm{Spitzer})}_{\mathrm{Cs\,Cs}} \approx 6.6\times10^{16}\,\mathrm{s}^{-1}$, which is over three orders of magnitude larger than the dense-plasma NYP value, $\nu^{(\mathrm{NYP})}_{\mathrm{Cs\,Cs}} \approx 2.4\times10^{13}\,\mathrm{s}^{-1}$. Regarding the electron–Cs ion collisions, one has $\nu^{(\mathrm{SK})}_{\mathrm{e\,Cs}} = \nu^{(\mathrm{Spitzer})}_{\mathrm{e\,Cs}} \approx 6.3\times10^{16}\,\mathrm{s}^{-1}$ at $T_\mathrm{e} = 100\,\mathrm{eV}$, but this corresponds to a mean free path $\lambda_{\mathrm{e\,Cs}} \approx 0.06\,\mathrm{nm} \ll r_\mathrm{Cs}$, so again the dense-plasma limit applies, which gives $\nu^{(\mathrm{NYP})}_{\mathrm{e\,Cs}} \approx 1.2\times10^{16}\,\mathrm{s}^{-1}$. The difference is even larger at the lower temperatures associated with the early-time interaction.

Moreover, the SK and NYP schemes handle colliding particles with non-equal statistical weights differently, which impacts the accuracy of energy conservation. However, that is likely not the cause of the diverging simulation results, since the number of computational particles is large in both cases, so as to limit statistical noise.

‖ Modifications to the implementation of the Sentoku & Kemp [37] collision model in Epoch over time make a direct comparison to TSR difficult.

¶ It should be emphasized though, that these PIC simulations are intrinsically classical, and as such, a self-consistent treatment of quantum effects is clearly outside their scope. Thus the extensions of any binary collision model to dense/cold plasma regions are ad-hoc models designed to reproduce plasma-averaged collisional properties expected from advanced warm-dense-matter or condensed-matter models [40].

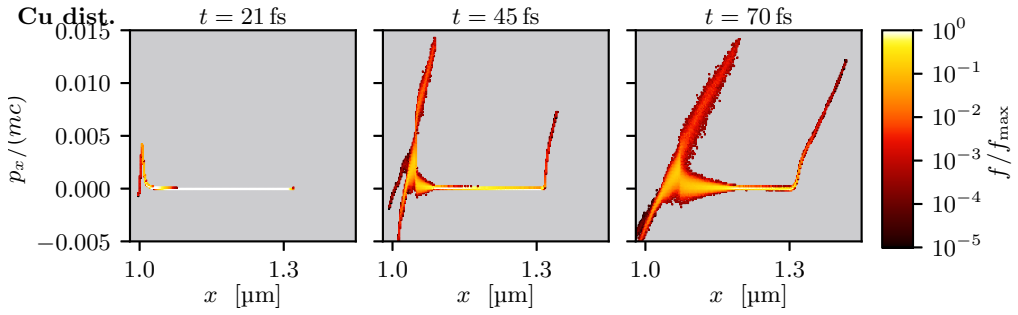


Figure 4. Copper ion phase-space distribution in the 300 nm thick Cu target from the collisional simulation, at times $t = 21$ fs, $t = 45$ fs and 70 fs.

A recent simulation study [42] of dense ($n_e = 60n_c$) plasmas driven at relativistic laser intensities, comparing the results of the SK and NYP[+] modules in EPOCH and the NYP module of Smilei, confirms that the SK model indeed results in stronger effective collisionality. In addition, a good agreement between EPOCH and Smilei was found when both employed the NYP algorithm.

Which of these two treatments of collisions in dense/cold plasmas is more physically correct is still a debated issue. Therefore, along with further numerical investigation, experimental verification should be sought for in order to determine the parameter regions of validity, and accuracy, of the two collision algorithms. Our results suggest that such differentiation between the algorithms is possible using laser-plasma experiments in multi-species, dense plasmas, such as the CsH case presented here. A good benchmarking test would be to compare ion energy spectra in cases where collisions are sufficiently strong to suppress ion reflection according to SK but not according to NYP. Such experiments might need to control the target density profile on the rear side, e.g. through laser ablation, in order to suppress TNSA, and make the shock accelerated ion population clearer. A potentially suitable experiment has recently been performed [18], but it would require further investigation to see whether the accuracy of the two models can be assessed from the obtained data (which clearly showed ion reflection).

4. Ion dynamics in copper targets

We will now turn to the pure copper simulations, first considering similar target and laser parameters to the CsH case, and subsequently changing these parameters one by one. The two main differences compared to CsH are the lack of multi-species effects and the ∼5 times higher electron density (assuming $Z^* = 27$). However, just as in the CsH target, the primary effect of collisions in the Cu plasma is the inverse Bremsstrahlung-type electron heating. The bulk electrons are heated to $T_e \approx 3.7$ keV, corresponding to a sound speed of $c_s \approx 1.3 \times 10^{-3}c$.

Figure 4 shows the collisional Cu ion phase-space distribution, at peak laser intensity ($t = 21$ fs), close after the laser irradiation ($t = 45$ fs), and even later in

[+] Since version `4.17` (June 2019) EPOCH has the full NYP algorithm implemented as well.

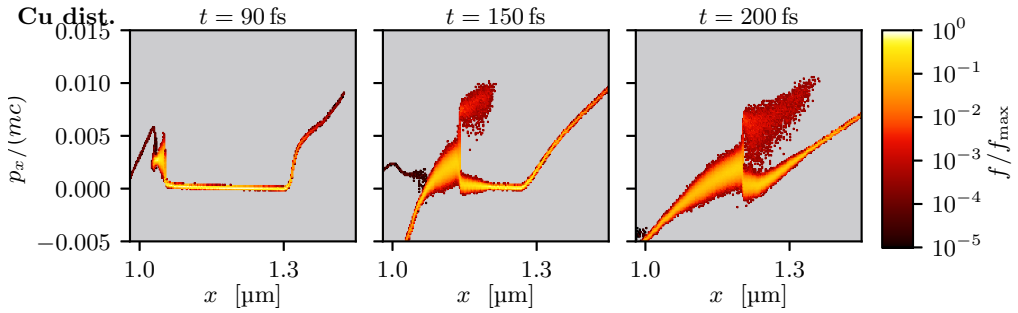


Figure 5. Copper ion phase-space distribution in the 300 nm thick Cu target from the collisional simulation, with an $a_0 = 10$ and 60 fs duration laser pulse. The distribution is shown at times $t = 90$ fs, $t = 150$ fs and 200 fs.

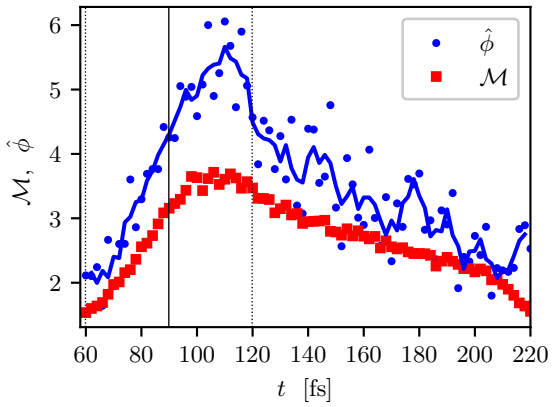


Figure 6. Temporal evolution of the normalized potential drop across the shock front, $\hat{\phi} = e\phi/T_e$, and shock Mach number, $\mathcal{M}$, for the thin copper target, long pulse collisional simulation. The blue line represents a moving average (over three data points) of $\hat{\phi}$. The vertical lines indicate the time of peak (solid) and half (dotted) laser intensity. For both the normalization of the potential and for the ion acoustic sound speed, an electron temperature of $T_e = 4$ keV was used as a representative value.

time ($t = 70$ fs). Similarly to Cs, the Cu ions have a rather low charge-to-mass ratio ($Z^*/A = 0.42$) and do not have time to fully respond to the laser piston during the short-pulse irradiation. Again, the initial perturbation from the laser piston transforms into an electrostatic shock, yet it is losing energy faster than in the CsH target.

Since the copper plasma does not contain any protons, all of the reflected charge, needed to sustain the shock, consists of Cu ions. Owing to their high charge ($Z^* = 27$), the collisional interaction between the reflected and the upstream ions is stronger than in the collisional CsH case, resulting in a noticeable heating of these two populations, as seen in the collisional Cu ion distributions at 45 fs and 70 fs in Fig. 4. Some heating is observed in the collisional proton and Cs ion distributions of Fig. 2 as well, but significantly weaker than in the copper plasma.

We have also studied a scenario wherein the copper plasma is illuminated by a laser pulse of longer duration (60 fs FWHM) and lower intensity ($a_0 = 10$). The Cu ion

phase-space distribution from the collisional simulation is displayed in Fig. 5, shown at times $t = 90\,\mathrm{fs}$ (at peak laser intensity), $t = 150\,\mathrm{fs}$ (close to the end of the pulse) and $t = 200\,\mathrm{fs}$. Like in the two previous setups, an electrostatic shock is generated. It forms out of a perturbation that detaches from the laser piston already as early as $t \approx 60\,\mathrm{fs}$, before the pulse has reached half its maximum intensity. It displays electrostatic shock-like properties, such as a sharp rise in lab-frame ion velocity in conjunction with a steep electrostatic potential barrier, but it lacks any ion reflection, as seen in the $t = 90\,\mathrm{fs}$ frame of the collisional simulation.

Figure 6 shows the evolution of the normalized* potential jump $\hat{\phi} = e\phi/T_\mathrm{e}$ and Mach number $\mathcal{M}$ of the shock from the time of detachment from the laser piston to its demise. The transition to a fully developed, ion-reflecting, electrostatic shock occurs when $\hat{\phi} \gtrsim \mathcal{M}^2/2$, which is at around $t \approx 90\,\mathrm{fs}$. The longer pulse duration and more gradual increase in intensity, detaches the onset of shock reflection from RPA.

The peaks in $\hat{\phi}$ and $\mathcal{M}$ are followed by a more gradual decrease in the Mach number and in the shock potential peak, starting at around $t \approx 110\,\mathrm{fs}$. The vertical lines in Fig. 6 represent the time of peak (solid) and half (dotted) laser intensity. The peaks thus occur before the laser intensity has halved. The delayed peaks in shock speed and potential relative to the peak laser intensity likely originate from the fact that the interaction has reached a stage where the laser is no longer able to supply more power than the energy dissipation rate of the shock.

The reflection of ions appears as a process bootstrapping itself. After the first few ions have been reflected, collisional heating between the upstream and reflected ions cause a broadening of the longitudinal momentum distribution of the upstream ions, leading to more ions entering the reflected region of phase-space. This upstream heating is seen in the collisional $t = 150\,\mathrm{fs}$ frame of Fig. 5. Towards the end of the simulation, the upstream and reflected ion populations start to merge into each other, after which the determination of the shock speed relative to the upstream population becomes unreliable. The shock ends somewhat abruptly when it collides with the rarefaction wave emanating from the back of the target, which occurs at roughly $t \approx 250\,\mathrm{fs}$.

As our final setup, we switch to a $2.5\,\mu\mathrm{m}$ copper target, driven by an $a_0 = 10$ and 60 fs FWHM duration pulse. Those parameters may be of interest to warm-dense-matter studies [29]. The simulation results are shown in Fig. 7. Despite the significant increase in target areal density, the measured electron temperature still reaches $T_\mathrm{e} \approx 3.5\,\mathrm{keV}$, thus the initial evolution of the shock is very similar to that in the thin-target simulation. Indeed, the Mach number and shock potential evolve as those displayed in Fig. 6, both qualitatively and quantitatively (when accounting for a time shift of $\simeq$15 fs corresponding to the different target position). The initial shock wave displays characteristic features of an electrostatic shock, such as ion reflection and a velocity modulation in the downstream. However, it also shows signs of a collisional

* Using a fixed value of $T_\mathrm{e} = 4\,\mathrm{keV}$, derived from Maxwellian fits to the electron energy spectrum (whole plasma). The measured electron temperature stays fairly close to this value during the entire duration of the pre-shock and the electrostatic shock.

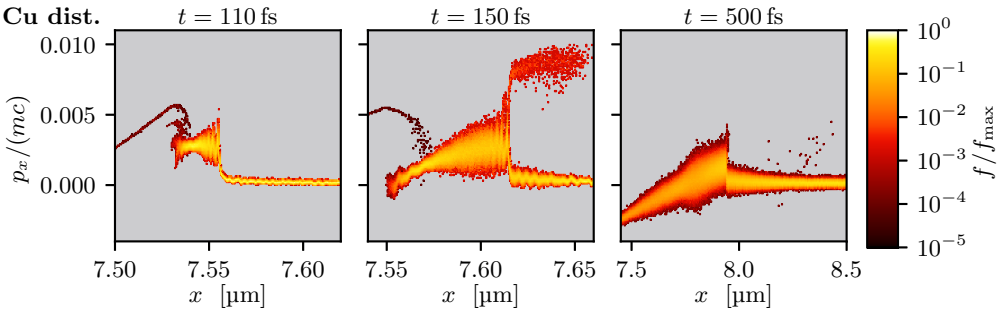


Figure 7. Distribution of copper ions in a 2.5 µm thick target, with collisions, at times $t = 110$ fs, $t = 150$ fs and 500 fs. Note that the initial position of the target front is at $x = 7.5$ µm, different from the other simulations presented.

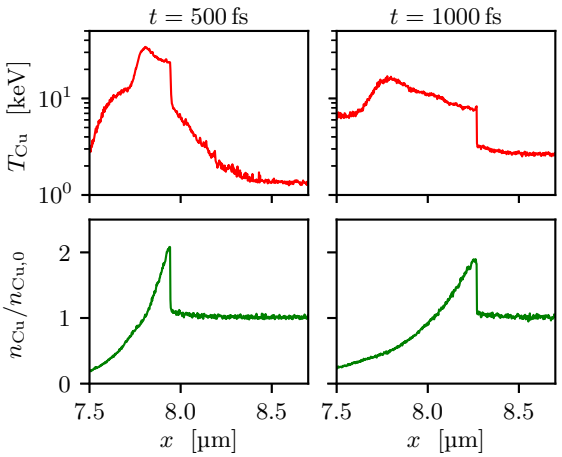


Figure 8. Spatial profiles of the copper ion temperature and density at $t = 500$ fs and $t = 1000$ fs. Both profiles display a sharp jump; the temperature jump by about a factor of 2.6, while the density jumps by about a factor 2.0.

shock, such as isotropization of the downstream ion distribution (i.e. the longitudinal and transverse temperatures are comparable to each other). The shock can therefore be claimed to be in a hybrid regime between a collisionless electrostatic shock and a hydrodynamic shock.

Since the target is now significantly thicker, the shock wave has time to further dissipate its energy, and the ion reflection terminates at $t \approx 300$ fs, well before the shock front encounters the rarefaction wave from the back of the target. As the shock steadily loses speed – and the electrostatic potential drop across the shock front decreases – a point is reached when the electrostatic potential barrier is too weak to cause ion reflection (in fact, the electric field reaches the level of statistical noise). However, even though the ion reflection is absent, the steady propagation of a clear shock front structure in phase space is clearly visible inside the target, in the $t = 500$ fs panel of Fig. 7. There are corresponding discontinuities in the ion temperature, T_{Cu}, and density, n_{Cu}, profiles: Figure 8 shows that T_{Cu} and n_{Cu} jump by a factor of 2.6 and 2.0, respectively. Since

the laser no longer exerts radiation pressure on the target front side, the latter rapidly expands towards the vacuum as a rarefaction wave propagates into the shocked plasma. At $t = 500\,\mathrm{fs}$, this rarefaction wave has caught up with the shock front to create a weakly supersonic ($\mathcal{M} \approx 1.3$), planar blast wave [43, Sec. 4.3], which slowly decays away (compare the ion temperature and density jumps at $t = 500\,\mathrm{fs}$ and $t = 1000\,\mathrm{fs}$).

To study how the qualitative features of the shock dynamics depend on laser parameters, further simulations have been performed; a_0 ranging from 2 to 14 and the pulse FWHM duration ranging from 15 fs to 120 fs. In addition, two simulations have been run with $a_0 = 7$ and 14, with the respective pulse durations varied such that the pulse energy would stay the same as in the case presented above ($a_0 = 10$ and 60 fs FWHM duration). We could identify two qualitatively different regimes for the ion dynamics. At lower intensities, the pulse is not strong enough to initiate ion reflection at any point; instead, a shock-like structure similar to the one displayed at $t = 110\,\mathrm{fs}$ in Fig. 7 is launched, and is sustained for several hundred femtoseconds, with its speed and amplitude decaying rather slowly. This behaviour is observed here for $a_0 \leq 7$, and also in the simulation with $a_0 = 7$ and 120 fs FWHM duration. The latter indicates that that both the laser intensity and energy are important for the onset of ion reflection.

At higher intensities, the behaviour is qualitatively similar to the one shown in Fig. 7 – ion reflection is initiated, followed by a gradual loss of energy, until ion reflection no longer occurs, and the shock turns into a collisionally sustained blast wave. However, the time scale for this transition to happen depends on the laser parameters: both higher intensity and shorter pulses result in an earlier onset of the ion reflection, as well as a faster transition into a blast wave. The reason for the faster demise of ion reflection may be linked to the rapid collisional heating of the upstream ions by the reflected ions. A hotter upstream favours ion reflection, thus hastening the shock dissipation. Remarkably, the ions in the downstream of the blast wave are heated to several tens of keV temperatures, in the first $\sim$100 fs after the ion reflection has ended. For instance, the temperature recorded in Fig. 8 is $\sim$20 keV at $t = 500\,\mathrm{fs}$. In the case of $a_0 = 14$ and FWHM duration of 30 fs, the downstream ion temperature reaches $\sim$60 keV at $t = 300\,\mathrm{fs}$, then dropping down to $\sim$30 keV at $t = 500\,\mathrm{fs}$. Unlike the heating scenario put forward by TSR [28], the heating process of the downstream heavy ions revealed by our simulations does not involve inter-species friction induced in the shock electrostatic potential.

Another trend observed in the scans is that shorter duration pulses generate faster shock evolution, i.e. a faster onset of ion refection, as well as a faster decay into a blast wave. This is also likely linked to the interaction of the laser piston and the plasma. Shorter laser pulses are quicker to reach their maximum intensity. The laser piston may therefore reach sufficient strength to reflect ions, before any pre-shock perturbation (e.g. as that in the $t = 110\,\mathrm{fs}$ panel in Fig. 7) would have time to form and overtake the piston. The early onset of ion reflection then leads to a rapid transition to a blast wave, as discussed in the previous paragraph.

In relation to the transition from hybrid shock to a blast wave, we note that the

end of the ion reflection is accompanied by an increase in the width of the shock front, from $\Delta x_{\rm sh} \sim 1.6\,$nm (i.e., a few times the Debye length $\lambda_{\rm D} \approx 0.3\,$nm) to $6{-}9\,$nm. This width is about an order of magnitude larger than the collisional ion mean free path, here estimated as the inter-atomic distance, $\lambda_{\rm mfp} \approx 0.25\,$nm. Our finding is consistent with previous estimates of the width of weakly supersonic ($\mathcal{M} \approx 2$) hydrodynamic shocks ($\Delta x_{\rm sh} \approx 20\lambda_{\rm mfp}$) [22, 44].

Finally, the robustness of the ion dynamics observed in the thick copper target has been tested against possible multidimensional effects on the laser-driven electron energization and subsequent ion dynamics, through a two-dimensional simulation of the thick copper target, detailed further in [29]. This simulation reveals that the situation studied here is sufficiently collisional that the shock does not suffer from transverse modulations.

5. Conclusions

Using particle-in-cell simulations, we have numerically investigated the impact of Coulomb collisions on the ion dynamics in high-Z^*, solid density caesium hydride and copper targets, irradiated by high-intensity ($I \approx 2{-}5 \times 10^{20}\,\mathrm{Wcm^{-2}}$), ultrashort ($10{-}60\,$fs), circularly polarized laser pulses.

In all cases collisional absorption through inverse Bremsstrahlung heats the electrons up to $3{-}10\,$keV temperatures throughout the target, while the use of CP reduces the creation of high-energy electrons. Subsequently, collisions quickly relax the electrons to a Maxwellian distribution. The impact of the laser pulse launches an electrostatic shock wave. In all cases studied here, the collisionally enhanced electron heating results in faster shock waves, with higher potential drops across the shock front, than in the corresponding collisionless simulations.

In the CsH target, the different charge-to-mass ratios of the hydrogen and caesium ions result in strong proton reflection. In contrast to the results of TSR [28], we do not observe a large number of protons passing through the shock front and get heated via collisional friction with the Cs ions. Instead, inter-species friction results in the *reflected* ions being heated up to $\sim$keV temperatures. The difference in proton reflection between our results and those of TSR appears to be a consequence of distinct collision models in the dense/cold plasmas where the Spitzer theory no longer applies. This suggests that laser plasma experiments, using targets containing a highly charged species and protons volumetrically, may be utilized to differentiate between numerical collision models.

In pure Cu targets, the collisional coupling between the reflected and upstream ions is stronger, causing an appreciable heating of these two. Also, the higher density of both ions and electrons causes a faster decay of the shock in the CsH target. When turning to a somewhat lower-intensity, but longer-duration laser pulse, the initial stages of the shock launching process become more decoupled from the laser pulse and the RPA. Here, the shock forms already prior to the on-target laser peak. However, the shock front continues to accelerate until about $\sim$20 fs after the on-target laser peak. Because

of the quick launch of the electrostatic shock, the maximum energy of the accelerated ions has less sharp temporal variation, since there is no transition from the RPA ions to the CSA ions. Yet, the shock initially lacks ion reflection, the onset of which appears to be bootstrapping itself via heating of the upstream ions by the reflected ones.

Lastly, we increased the target thickness in order to follow the electrostatic shock evolution over a longer duration, and to become more relevant to high-energy-density-physics applications. While the shock wave is at no point purely electrostatic, as it exhibits some features of hydrodynamic shocks, we observe the shock speed and potential drop to decay until the shock loses its capability to reflect ions. At this stage, the electrostatic potential drop across the shock front has also disappeared, and a rarefaction wave launched from the target front side has overtaken the shock front, turning it into a weakly supersonic ($\mathcal{M} \approx 1.3$) collisional blast wave. This formation is capable of locally heating up the downstream ions to tens of keV temperatures for a duration of about $\sim$100 fs.

Acknowledgments

The authors are grateful for fruitful discussions with L. Hesslow and T. Fülöp, as well as to M. Grech and F. Pérez for support with Smilei, and A. E. Turrel for providing inputs for simulations presented in [28]. This project has received funding from the European Research Council (ERC) under the European Union's Horizon 2020 research and innovation programme under grant agreement No 647121, the Swedish Research Council (grant no. 2016-05012), and the Knut och Alice Wallenberg Foundation. The simulations were performed on resources provided by the Swedish National Infrastructure for Computing (SNIC) at Chalmers Centre for Computational Science and Engineering (C^3SE) and High Performance Computing Center North (HPC^2N).

References

[1] Macchi A, Borghesi M and Passoni M 2013 *Rev. Mod. Phys.* **85**(2) 751–793

[2] Borghesi M, Campbell D H, Schiavi A, Haines M G, Willi O, MacKinnon A J, Patel P, Gizzi L A, Galimberti M, Clarke R J, Pegoraro F, Ruhl H and Bulanov S 2002 *Physics of Plasmas* **9** 2214–2220

[3] Romagnani L, Fuchs J, Borghesi M, Antici P, Audebert P, Ceccherini F, Cowan T, Grismayer T, Kar S, Macchi A, Mora P, Pretzler G, Schiavi A, Toncian T and Willi O 2005 *Phys. Rev. Lett.* **95**(19) 195001

[4] Patel P K, Mackinnon A J, Key M H, Cowan T E, Foord M E, Allen M, Price D F, Ruhl H, Springer P T and Stephens R 2003 *Phys. Rev. Lett.* **91**(12) 125004

[5] Dyer G M, Bernstein A C, Cho B I, Osterholz J, Grigsby W, Dalton A, Shepherd R, Ping Y, Chen H, Widmann K and Ditmire T 2008 *Phys. Rev. Lett.* **101**(1) 015002

[6] Mančić A, Lévy A, Harmand M, Nakatsutsumi M, Antici P, Audebert P, Combis P, Fourmaux S, Mazevet S, Peyrusse O, Recoules V, Renaudin P, Robiche J, Dorchies F and Fuchs J 2010 *Phys. Rev. Lett.* **104**(3) 035002

[7] Roth M, Jung D, Falk K, Guler N, Deppert O, Devlin M, Favalli A, Fernandez J, Gautier D, Geissel M, Haight R, Hamilton C E, Hegelich B M, Johnson R P, Merrill F, Schaumann G,

Schoenberg K, Schollmeier M, Shimada T, Taddeucci T, Tybo J L, Wagner F, Wender S A, Wilde C H and Wurden G A 2013 *Phys. Rev. Lett.* **110**(4) 044802

[8] Dromey B, Coughlan M, Senje L, Taylor M, Kuschel S, Villagomez-Bernabe B, Stefanuik R, Nersisyan G, Stella L, Kohanoff J *et al.* 2016 *Nat. Commun.* **7** 10642

[9] Barberio M, Scisciò M, Vallières S, Cardelli F, Chen S, Famulari G, Gangolf T, Revet G, Schiavi A, Senzacqua M *et al.* 2018 *Nat. Commun.* **9** 372

[10] Higginson D, Korneev P, Ruyer C, Riquier R, Moreno Q, Béard J, Chen S, Grassi A, Grech M, Gremillet L *et al.* 2019 *Commun. Phys.* **2** 1–7

[11] Bulanov S, Esirkepov T, Khoroshkov V, Kuznetsov A and Pegoraro F 2002 *Physics Letters A* **299** 240 – 247

[12] Linz U and Alonso J 2007 *Phys. Rev. ST Accel. Beams* **10**(9) 094801

[13] Denavit J 1992 *Phys. Rev. Lett.* **69** 3052–3055

[14] Silva L O, Marti M, Davies J R, Fonseca R A, Ren C, Tsung F S and Mori W B 2004 *Phys. Rev. Lett.* **92**(1) 015002

[15] Romagnani L, Bulanov S V, Borghesi M, Audebert P, Gauthier J C, Löwenbrück K, Mackinnon A J, Patel P, Pretzler G, Toncian T and Willi O 2008 *Phys. Rev. Lett.* **101** 025004

[16] Haberberger D, Tochitsky S, Fiuza F, Gong C, Fonseca R A, Silva L O, Mori W B and Joshi C 2012 *Nat. Phys.* **8** 95–99

[17] Fiuza F, Stockem A, Boella E, Fonseca R A, Silva L O, Haberberger D, Tochitsky S, Gong C, Mori W B and Joshi C 2012 *Phys. Rev. Lett.* **109**(21) 215001

[18] Pak A, Kerr S, Lemos N, Link A, Patel P, Albert F, Divol L, Pollock B B, Haberberger D, Froula D, Gauthier M, Glenzer S H, Longman A, Manzoor L, Fedosejevs R, Tochitsky S, Joshi C and Fiuza F 2018 *Phys. Rev. Accel. Beams* **21** 103401

[19] Karimabadi H, Roytershteyn V, Vu H X, Omelchenko Y A, Scudder J, Daughton W, Dimmock A, Nykyri K, Wan M, Sibeck D, Tatineni M, Majumdar A, Loring B and Geveci B 2014 *Physics of Plasmas* **21** 062308

[20] Dieckmann M E, Doria D, Sarri G, Romagnani L, Ahmed H, Folini D, Walder R, Bret A and Borghesi M 2017 *Plasma Physics and Controlled Fusion* **60** 014014

[21] Perkins L J, Betti R, LaFortune K N and Williams W H 2009 *Phys. Rev. Lett.* **103**(4) 045004

[22] Bellei C, Rinderknecht H, Zylstra A, Rosenberg M, Sio H, Li C K, Petrasso R, Wilks S C and Amendt P A 2014 *Physics of Plasmas* **21** 056310

[23] Santos J J, Vauzour B, Touati M, Gremillet L, Feugeas J L, Ceccotti T, Bouillaud R, Deneuville F, Floquet V, Fourment C, Hadj-Bachir M, Hulin S, Morace A, Nicolaï P, d'Oliveira P, Reau F, Samaké A, Tcherbakoff O, Tikhonchuk V T, Veltcheva M and Batani D 2017 *New Journal of Physics* **19** 103005

[24] Spitkovsky A 2008 *The Astrophysical Journal* **682** L5–L8

[25] Lemoine M, Gremillet L, Pelletier G and Vanthieghem A 2019 *Phys. Rev. Lett.* **123**(3) 035101

[26] Stockem A, Fiuza F, Bret A, Fonseca R and Silva L 2014 *Scientific reports* **4** 3934

[27] Sundström A, Juno J, TenBarge J M and Pusztai I 2019 *J. Plasma Phys.* **85**(1) 905850108

[28] Turrell A E, Sherlock M and Rose S J 2015 *Nat. Commun.* **6** 8905

[29] Sundström A, Siminos E, Gremillet L and Pusztai I 2020 *Journal of Plasma Physics* **86**(2) 755860201

[30] Derouillat J, Beck A, Pérez F, Vinci T, Chiaramello M, Grassi A, Flé M, Bouchard G, Plotnikov I, Aunai N, Dargent J, Riconda C and Grech M 2018 *Comput. Phys. Commun.* **222** 351

[31] Pérez F, Gremillet L, Decoster A, Drouin M and Lefebvre E 2012 *Phys. of Plasmas* **19** 083104

[32] Kruer W L and Estabrook K 1985 *The Phys. of Fluids* **28** 430–432

[33] Bauer D and Mulser P 2007 *Physics of Plasmas* **14** 023301

[34] May J, Tonge J, Fiuza F, Fonseca R A, Silva L O, Ren C and Mori W B 2011 *Phys. Rev. E* **84** 025401

[35] Pusztai I, TenBarge J M, Csapó A N, Juno J, Hakim A, Yi L and Fülöp T 2018 *Plasma Physics and Controled Fusion* **60** 035004

[36] Arber T D, Bennett K, Brady C S, Lawrence-Douglas A, Ramsay M G, Sircombe N J, Gillies P, Evans R G, Schmitz H, Bell A R and Ridgers C P 2015 *Plasma Physics and Controlled Fusion* **57** 113001
[37] Sentoku Y and Kemp A 2008 *J. of Comput. Phys.* **227** 6846–6861
[38] Nanbu K 1997 *Phys. Rev. E* **55**(4) 4642–4652
[39] Nanbu K and Yonemura S 1998 *Journal of Computational Physics* **145** 639 – 654 ISSN 0021-9991
[40] Dharma-wardana M W C, Klug D D, Harbour L and Lewis L J 2017 *Phys. Rev. E* **96**(5) 053206
[41] Lee Y T and More R M 1984 *The Physics of Fluids* **27** 1273–1286
[42] Bhadoria S, Kumar N and Keitel C H 2019 Stable quasi-monoenergetic ion acceleration from the laser-driven shocks in a collisional plasma *Version 2 contains a comparison between two PIC collision algorithms.* (*Preprint* `https://arxiv.org/abs/1707.03309v2`)
[43] Drake R P 2006 *High Energy Density Physics: Fundamentals, Inertial Fusion and Experimental Astrophysics* (Berlin Heidelberg: Springer-Verlag) ISBN 978-3-540-29315-6
[44] Vidal F, Matte J P, Casanova M and Larroche O 1993 *Physics of Fluids B: Plasma Physics* **5** 3182–3190